

NJC

Accepted Manuscript



This is an *Accepted Manuscript*, which has been through the Royal Society of Chemistry peer review process and has been accepted for publication.

Accepted Manuscripts are published online shortly after acceptance, before technical editing, formatting and proof reading. Using this free service, authors can make their results available to the community, in citable form, before we publish the edited article. We will replace this *Accepted Manuscript* with the edited and formatted *Advance Article* as soon as it is available.

You can find more information about *Accepted Manuscripts* in the [Information for Authors](#).

Please note that technical editing may introduce minor changes to the text and/or graphics, which may alter content. The journal's standard [Terms & Conditions](#) and the [Ethical guidelines](#) still apply. In no event shall the Royal Society of Chemistry be held responsible for any errors or omissions in this *Accepted Manuscript* or any consequences arising from the use of any information it contains.

Cite this: DOI: 10.1039/c0xx00000x

www.rsc.org/xxxxxx

ARTICLE TYPE

New insights into the role of lattice oxygen in the catalytic carbonization of polypropylene into high value-added carbon nanomaterials†

Jiang Gong,^{a,b} Jie Liu,^a Zhiwei Jiang,^a Xuecheng Chen,^{*,a,c} Xin Wen,^a Ewa Mijowska,^c and Tao Tang^{*,a}

Received (in XXX, XXX) Xth XXXXXXXXXX 200X, Accepted Xth XXXXXXXXXX 200X

DOI: 10.1039/b000000x

Catalytic conversion of waste plastics into high value-added carbon nanomaterials (CNMs) has attracted increasing attention; however, the role of lattice oxygen in the carbonization of plastics still remains ambiguous. In this work, firstly, nickel catalyst with different content of lattice oxygen was prepared by sol-gel combustion synthesis method. Subsequently, the effect of lattice oxygen in nickel catalyst on the catalytic carbonization of polypropylene (PP, an example of plastics) into CNMs was investigated. It was found that the yield of CNMs increased dramatically with the increasing content of lattice oxygen. Large and short platelet-like carbon fibers were obtained when the content of lattice oxygen was low. With the increasing content of lattice oxygen, small, winding and short carbon nanofibers were produced. When the content of lattice oxygen further increased, long, small and straight cup-stacked carbon nanotubes were formed. Besides, it was demonstrated that lattice oxygen not only prevented the coalescence of nickel catalyst nanoparticles into large particles and promoted their reconstruction into rhombic shape, but also facilitated the catalytic carbonization of PP degradation products. This work provides new insights into the carbonization mechanism of plastics and puts forward a novel chemical method to prepare CNMs with diverse morphologies by controlling the content of lattice oxygen in catalyst.

1. Introduction

The catalytic conversion of waste plastics into something useful and more valuable has aroused much interest,¹⁻³ owing to the ever-increasing generation of waste plastics (*e.g.*, more than 25 million tons of waste plastics were generated in Europe in 2011). Chemical recycling can recover the petrochemical components of waste plastics, which could be used to produce other synthetic chemicals.^{4,5} However, the development of a new economically feasible chemical recycling process is still of great importance for waste plastics treatment. Waste polyolefin is the main component among waste plastics, and the content of carbon in polyolefin is about 85.7 wt %. Thereby, catalytic carbonization of polyolefin into high value-added carbon nanomaterials (CNMs) will open up new avenues for deep processing and comprehensive utilization of waste plastics.

So far, many studies have been conducted to transform virgin or waste polyolefin including polypropylene (PP) and polyethylene (PE) into CNMs such as carbon nanotubes (CNTs), cup-stacked CNTs (CS-CNTs), carbon nanofibers (CNFs) and carbon spheres (CSs). Wu *et al.* used catalytic gasification to process PP into CNTs and hydrogen-rich synthetic gas by Ni/Ca-Al or Ni/Zn-Al catalyst.^{6,7} Acomb *et al.* used pyrolysis-gasification of PP and PE to prepare CNTs by Ni/Al₂O₃ catalyst.⁸ Zhuo *et al.* reported the synthesis of CNTs from PE using a pyrolysis-combustion technique.^{9,10} Recently, they found that the oxidative heat treatment of stainless steel favored for the production of CNTs.¹¹ Pol *et al.* used autoclave as reactor to

convert PE into CNTs and CSs under high pressure.¹² Our group put forward a strategy of combined degradation catalyst/carbonization catalyst, including solid acid, halogenated compound or activated carbon/nickel (or cobalt) catalyst, to convert plastics into CNTs, CS-CNTs, CNFs and CSs under atmospheric condition.¹³⁻²¹ The resultant CNMs could be used in a lot of fields such as heterogeneous catalysis¹⁷ and environment remediation.¹⁹

Undoubtedly, the high-yield conversion of plastics into CNTs is more challenging than in the case using simple one light hydrocarbon as carbon source, because the degradation products of plastics are complicated and consist of light hydrocarbons, aromatics and long-chain olefins.^{16,19,20} As well known, the maintenance of high catalytic activity of catalyst is crucial to improve the yield of CNTs. Previous work showed that the addition of water or other oxygen-containing compound could clean off the amorphous carbon coating around catalyst, which promoted the growth of CNTs.^{6-8,22-24} Janowska *et al.* recently demonstrated that the growth rate and quality of vertically aligned CNTs were significantly improved by addition of small amount of ethanol (*e.g.*, 9 vol %).²⁵ Other common strategy to enhance the catalytic activity of catalyst is to add the second metal element or utilize the lattice oxygen in catalyst itself. Pfefferle *et al.* reported that the addition of Cr or Mn element into Co-MCM-41 catalyst increased the selectivity and yield of single-walled CNTs.²⁶⁻²⁸ Liu *et al.* demonstrated that oxygen atom in SiO_x nanoparticle enhanced the capture of -CH_x and facilitated the growth of single-walled CNTs.²⁹ Qian *et al.* found

that the lattice oxygen in the unreduced Co-Mo/Al₂O₃ consumed part of hydrogen and carbon (to the H₂O and CO), making the equilibrium of methane decomposition shift to the direction of hydrogen and CNTs production in a much higher reaction rate.³⁰ However, they did not investigate the influence of lattice oxygen on the yield, morphology and microstructure of CNTs, nor study the effect of lattice oxygen on the coalescence and reconstruction of catalyst, which are of great significance to uncover the role of lattice oxygen in the formation of CNTs and improve the yield of CNTs. Recently, we found that the nano-sized NiO prepared from sol-gel combustion synthesis method could catalyze the degradation products of PP or PE into long, straight and smooth-surface CS-CNTs, in which the coalescence and reconstruction of NiO nanoparticles into rhombic shape were the vital steps.^{16,18,19} The previous work prompted us to think about further questions: How does the content of lattice oxygen in NiO catalyst influence the yield, morphology and microstructure of CNMs? How does the lattice oxygen affect the coalescence and reconstruction of NiO nanoparticles and the carbonization of PP degradation products? Solving these problems will not only help to improve the yield of CNMs and provide more insights into the carbonization mechanism of polyolefin, but also contribute to the conversion of waste polyolefin into valuable CNMs.

On the other hand, although CNMs with diverse morphologies have been prepared from plastics,⁶⁻²¹ to the best of our knowledge, there are no reports about synthesizing platelet-like carbon fibers (PL-CFs) using plastics as carbon sources. PL-CFs have attracted a great deal of research attention due to their special stacked morphology consisting of many platelet-like graphene layers perpendicularly to the fiber axis. They are different from conventional CNTs made up of multi-seamless cylinders of hexagonal carbon networks or CNFs composed of random orientation graphene layers. Such a special microstructure provides a large portion of exposed and reactive edges on the surface of PL-CFs,³¹ and makes them potential candidates in lithium ion batteries,³¹ fuel cells,^{32,33} and heterogeneous catalysis.^{34,35} As a result, the synthesis of PL-CFs from plastics is highly desirable.

Herein, firstly, nano-sized nickel catalyst with different content of lattice oxygen was prepared by sol-gel combustion synthesis method. Subsequently, the combined CuBr/nickel catalyst was used to catalyze carbonization of PP into CNMs including PL-CFs, CNFs and CS-CNTs at 700 °C. The effects of the content of lattice oxygen in nickel catalyst on the yield, morphology, microstructure, phase structure and thermal stability of CNMs were investigated. Besides, the effects of lattice oxygen on the coalescence and reconstruction of nickel catalyst nanoparticles and the carbonization of PP degradation products were explored. Finally, a possible mechanism was proposed to expound the role of lattice oxygen in the catalytic carbonization of PP into CNMs with diverse morphologies.

2. Experimental

2.1 Materials

Polypropylene (PP, weight-average molecular weight = 3.07×10^5 g/mol, polydispersity index = 3.13, and trademark T30S) powder was supplied by Yanan Petrochemical Co., China. Nano-

sized nickel catalyst with different content of lattice oxygen was prepared by sol-gel combustion synthesis method according to the previous report.³⁶ Briefly, precursor solution was prepared as following: 0.10 mol Ni(NO₃)₂·6H₂O (analytical reagent, supplied from Beijing Chemical Works) and a designed amount of citric acid (simplified as CA, analytical reagent, provided by Beijing Chemical Works) were dissolved in 200 mL deionized water. The pH value of solution was adjusted to 7 by ammonia (analytical reagent, supplied from Beijing Chemical Works). The solution was evaporated at 95 °C until forming gel, which was further heated under the protection of nitrogen gas at the temperature of self-ignition. The obtained nickel catalyst was designated as Cat-x, where x represented the molar ratio of Ni(NO₃)₂ to CA in the precursor solution, and used as carbonization catalyst to synthesize CNMs. CuBr was of analytical grade and purchased from Beijing Chemical Works.

2.2 Preparation of samples

PP powder (40.00 g) was mixed with Cat-x (1.00, 2.00 or 3.00 g) and CuBr (0.050 g) in a Brabender mixer at 100 rpm and 180 °C for 8 min. The resultant sample was denoted as PP/CuBr-Cat-x-y, where y represented the content of Cat-x (g/100 g PP). For comparison, PP/CuBr with CuBr content of 0.125 (g/100 g PP) and PP/Cat-x-y were also prepared.

2.3 Preparation of CNMs

CNMs were prepared through carbonization experiment by heating PP/CuBr-Cat-x-y in a crucible at 700 °C according to our previous reports.^{14,17} Briefly, a piece of PP/CuBr-Cat-x-y (about 5.0 g) was placed into a crucible, which was heated at 700 °C for about 5 min. The resultant CNMs were cooled to room temperature, weighed and designated as CNMy-z, where z represented the content of lattice oxygen (mol/100 mol Ni) in the Cat-x. The yield of CNMs was calculated by dividing the amount of the obtained carbon (the amount of the residue after subtracting the amount of the residual catalysts) by that of carbon element in the PP from PP/CuBr-Cat-x-y. Each measurement was repeated four times for reproducibility purpose.

2.4 Characterization

The morphologies of Cat-x and CNMs were observed by field-emission scanning electron microscope (FE-SEM, XL30ESEM-FEG) and transmission electron microscope (TEM, JEM-1011) at an accelerating voltage of 100 kV. The microstructure of CNMs was investigated using high-resolution TEM (HRTEM) performed on a FEI Tecnai G2 S-Twin transmission electron microscope operating at 200 kV. The phase structures of Cat-x and CNMs were analyzed by X-ray diffraction (XRD) using a D8 advance X-ray diffractometer with Cu K α radiation operating at 40 kV and 200 mA. The vibrational property of CNMs was characterized by Raman spectroscopy (T6400, excitation-beam wavelength: 514.5 nm). The thermal stabilities of Cat-x and CNMs were measured by thermal gravimetric analysis (TGA) under air flow at a heating rate of 10 °C/min using a TA Instruments SDT Q600.

3. Results and discussion

3.1 Characterization of nickel catalysts

Nickel catalysts were synthesized by sol-gel combustion synthesis method. FE-SEM images revealed that the resultant nickel catalysts had lamellar structure ranging from hundreds of nanometers to several micrometers in length (see Fig. S1 in the ESI†). When the molar ratio of $\text{Ni}(\text{NO}_3)_2$ to CA increased, the lamella of nickel catalysts became thinner. TEM images of nickel catalysts (Fig. 1) demonstrated that they consisted of uniform nanoparticles. The size distribution histograms of nickel catalyst nanoparticles are shown in Fig. S2. The average diameter was 25.2 ± 3.2 nm for Cat-1.0, 23.6 ± 2.2 nm for Cat-1.25, 23.7 ± 2.6 nm for Cat-1.67, 24.9 ± 2.5 nm for Cat-2.5, 17.6 ± 2.5 nm for Cat-3.33, and 17.5 ± 2.4 nm for Cat-5.0. That is to say, the size of the synthesized nickel catalysts was similar.

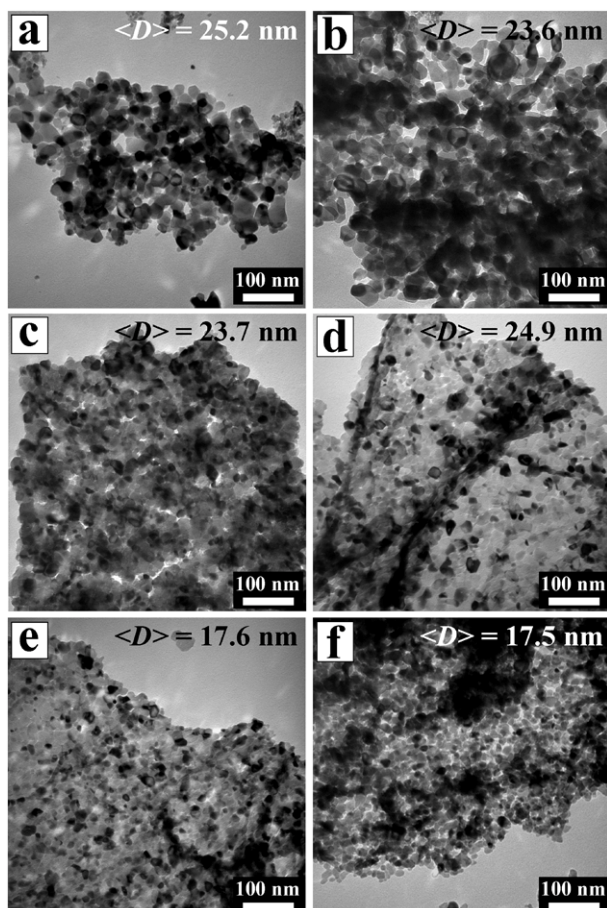


Fig. 1 TEM images of nickel catalysts: (a) Cat-1.0, (b) Cat-1.25, (c) Cat-1.67, (d) Cat-2.5, (e) Cat-3.33 and (f) Cat-5.0.

XRD patterns of nickel catalysts are shown in Fig. 2. For Cat-1.0, Cat-1.25, Cat-1.67 and Cat-2.5, characteristic diffraction peaks of metallic nickel were clearly observed at $2\theta = 44.8^\circ$ (111), 52.1° (200) and 76.6° (220), suggesting that they contained metallic nickel nanoparticles. However, characteristic diffraction peaks of NiO at $2\theta = 37.6^\circ$ (111), 43.6° (200), 63.2° (220), 75.7° (311) and 79.7° (222) were also observed in Cat-1.25, Cat-1.67 and Cat-2.5, indicating that they also contained NiO nanoparticles. These characteristic diffraction peaks of NiO became stronger when the molar ratio of $\text{Ni}(\text{NO}_3)_2$ to CA increased, implying that the content of NiO in the nickel catalysts increased. Moreover, when the molar ratio of $\text{Ni}(\text{NO}_3)_2$ to CA further increased to 3.33 or 5.0, the characteristic diffraction peaks of metallic nickel

disappeared, and only characteristic diffraction peaks of NiO remained, demonstrating that Cat-3.33 and Cat-5.0 were composed of NiO nanoparticles.

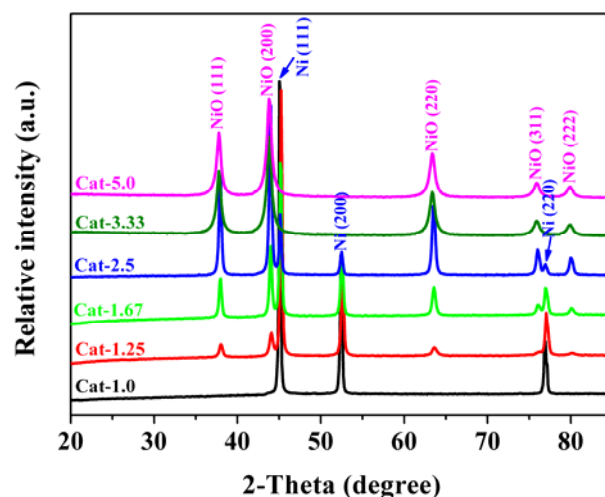


Fig. 2 XRD patterns of nickel catalysts.

Fig. S3 shows the TGA and derivative TGA (DTG) curves of Cat-x under air flow at a heating rate of $10^\circ\text{C}/\text{min}$. The weight increase from 400 to 900°C was due to the oxidation of Ni to NiO. Cat-1.0, Cat-1.25, Cat-1.67 and Cat-2.5 showed the maximum oxidation temperature at 682.6 , 616.9 , 603.0 and 511.1°C , respectively, and the corresponding weight increase at 900°C was 25.1 , 20.8 , 13.7 and 3.1 wt %, respectively. However, Cat-3.33 and Cat-5.0 showed no maximum oxidation temperature, and the weight at 900°C decreased by 2.1 and 2.2 wt %, respectively, which was probably caused by the decomposition of impurities. The content of lattice oxygen in Cat-x was calculated according to the weight change of Cat-x at 900°C , and the results are shown in Fig. 3. The content of lattice oxygen (mol/100 mol Ni) was 0 for Cat-1.0, 15.6 for Cat-1.25, 41.7 for Cat-1.67, 80.6 for Cat-2.5, 99.6 for Cat-3.33, and 100 for Cat-5.0.

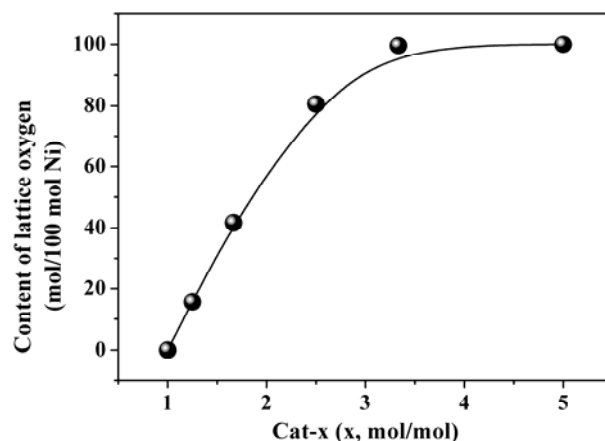


Fig. 3 The content of lattice oxygen in the nickel catalysts.

3.2 Effect of lattice oxygen on the yield of CNMs

In the cases of PP/CuBr and PP/Cat-x-y, the yield of CNMs was less than 1.0 and 5.1 wt %, respectively, indicating that CuBr or Cat-x alone could not effectively catalyze carbonization of PP. Fig. 4 shows the effect of the content of lattice oxygen on the

yield of CNMs from PP/CuBr-Cat-x-y. Interestingly, after adding 0.125 (g/100 g PP) CuBr into PP/Cat-x-y, the yield of CNMs from PP/CuBr-Cat-x-y increased obviously with the increasing content of lattice oxygen, regardless of Cat-x content (2.5, 5.0 or 7.5 g/100 g PP). Taking PP/CuBr-Cat-x-7.5 as an example, the yield of CNM7.5-z increased from 7.4 to 63.4 wt %, when the content of lattice oxygen in Cat-x increased from 0 to 100 (mol/100 mol Ni). As a consequence, the content of lattice oxygen in Cat-x played an important role in the catalytic carbonization of PP into CNMs. In addition, when the content of Cat-x increased from 2.5 to 7.5 (g/100 g PP), the yield of CNMs increased. For example, the yield of CNMy-100 from PP/CuBr-Cat-5.0-y increased from 33.0 to 63.4 wt %, much more significantly than that of CNMy-0 from PP/CuBr-Cat-1.0-y. Accordingly, the combined CuBr/Cat-5.0 showed much higher catalytic efficiency than CuBr/Cat-1.0 in the catalytic carbonization of PP, indicating that the catalytic ability of Cat-5.0 was much higher than that of Cat-1.0, since the carbon sources (*i.e.*, the degradation products of PP under the catalysis of CuBr) were the same. More discussion about the effect of lattice oxygen in Cat-x on the carbonization of PP degradation products will be provided in Section 3.6.

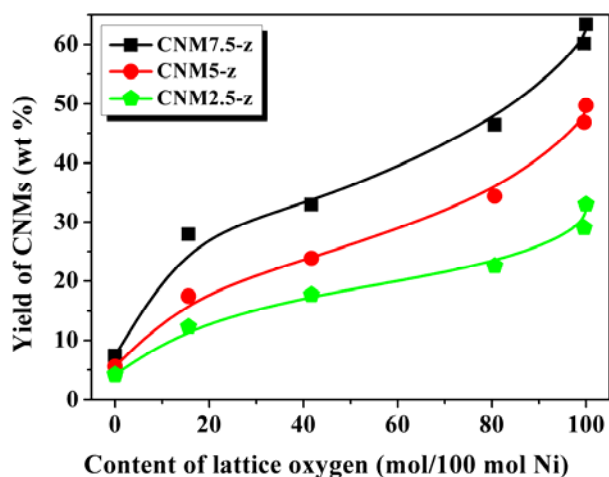


Fig. 4 Effect of the content of lattice oxygen in Cat-x on the yield of CNMs from PP/CuBr-Cat-x-y at 700 °C.

3.3 Effects of lattice oxygen on the morphology and microstructure of CNMs

To investigate whether the lattice oxygen in nickel catalyst had any effects on the morphology and microstructure of CNMs, FE-SEM, TEM and HRTEM observations were performed on the resultant CNM7.5-z from PP/CuBr-Cat-x-7.5. Fig. 5 shows the FE-SEM images of the CNM7.5-z. Strikingly, when the content of lattice oxygen in nickel catalyst was low, a lot of thick and short filamentous carbon was obtained in the CNM7.5-0 and CNM7.5-15.6 (Figs. 5a and 5b). However, when the content of lattice oxygen in nickel catalyst increased to 41.7 or 80.6 (mol/100 mol Ni), filamentous carbon in the resultant CNM7.5-41.7 or CNM7.5-80.6 became smaller, and the length showed no obvious changes (Figs. 5c and 5d). Interestingly, when the content of lattice oxygen further increased to 99.6 or 100 (mol/100 mol Ni), there was a great amount of relatively straight, smaller and long filamentous carbon in the obtained CNM7.5-

99.6 or CNM7.5-100 (Figs. 5e and 5f).

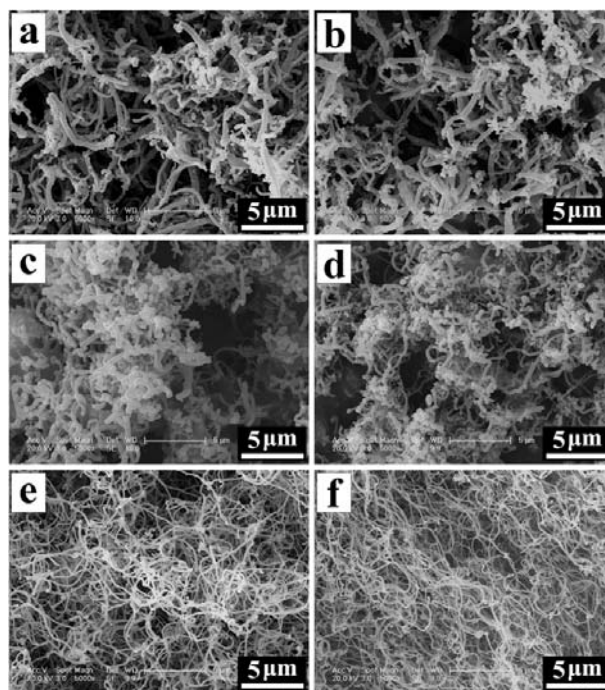


Fig. 5 FE-SEM images of CNMs: (a) CNM7.5-0, (b) CNM7.5-15.6, (c) CNM7.5-41.7, (d) CNM7.5-80.6, (e) CNM7.5-99.6 and (f) CNM7.5-100.

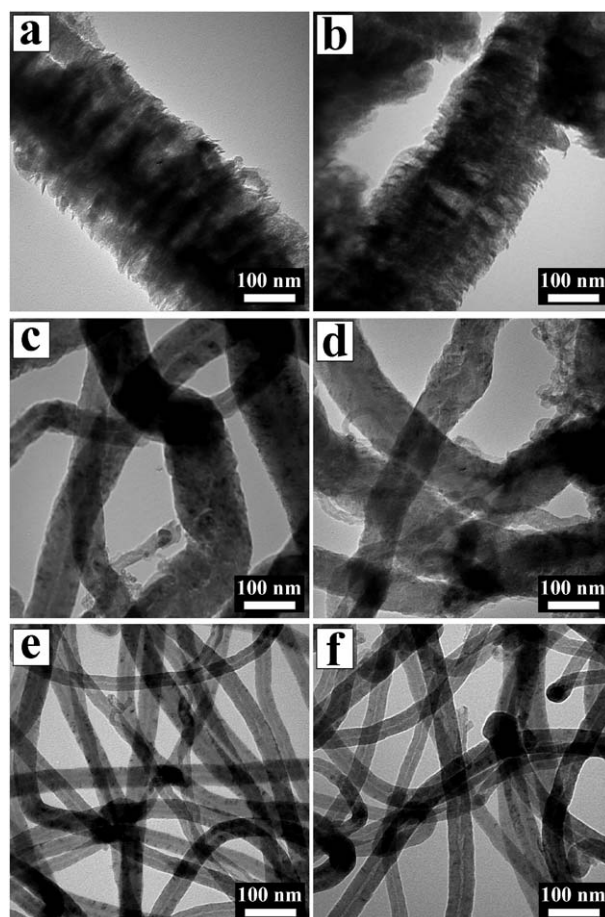


Fig. 6 TEM images of CNMs: (a) CNM7.5-0, (b) CNM7.5-15.6, (c) CNM7.5-41.7, (d) CNM7.5-80.6, (e) CNM7.5-99.6 and (f) CNM7.5-100.

Fig. 6 displays the TEM images of the corresponding CNMs. Large and short CFs with wide diameter and length distributions were found in both CNM7.5-0 and CNM7.5-15.6 (Figs. 6a, 6b, S4 and S5), and the surface of CFs was rough. The mean outer diameter and length of CNM7.5-0 and CNM7.5-15.6 were 362 nm and 3.6 μm , and 353 nm and 4.1 μm , respectively (Fig. 7). Comparatively, small, winding and short CNFs were obtained in both CNM7.5-41.7 and CNM7.5-80.6 (Figs. 6c, 6d, S4 and S5), of which the mean outer diameter and length were 84.8 nm and 5.8 μm , and 81.5 nm and 6.0 μm , respectively (Fig. 7). Strikingly, the resultant straight and long filamentous carbon from CNM7.5-99.6 and CNM7.5-100 had a tubular-like form (Figs. 6e and 6f), which is characteristic of CNTs. The surface of CNTs seemed to be smooth, and they had narrow diameter and length distributions (Figs. S4 and S5). The mean outer diameter and length were 42.6 nm and 10.8 μm for CNM7.5-99.6, and 38.3 nm and 11.8 μm for CNM7.5-100 (Fig. 7).

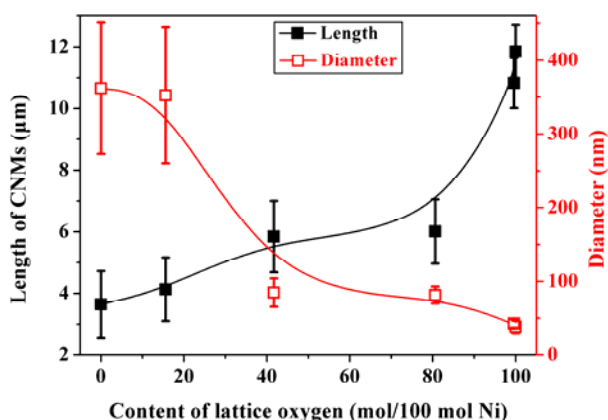


Fig. 7 Effects of the content of lattice oxygen on the length and diameter of CNMs from PP/CuBr-Cat-x-7.5 at 700 $^{\circ}\text{C}$.

To further clarify the effect of lattice oxygen in nickel catalyst on the microstructures of the resultant CFs, CNFs and CNTs, HRTEM observations were conducted on the CNM7.5-0, CNM7.5-41.7 and CNM7.5-100. Interestingly, the HRTEM image (Fig. 8a) of CNM7.5-0 showed that the large and short CFs were composed of many edge-exposed graphene platelets almost perpendicularly to the fiber axis. The special platelet-like structure demonstrated that CNM7.5-0 were PL-CFs, which could be used in the applications of lithium ion batteries,³¹ fuel cells,^{32,33} and heterogeneous catalysis.^{34,35} The interlayer spacing between graphitic layers was in the range of 0.34–0.36 nm, and the graphitic layers were discontinuous and had many defects, suggesting the low graphitization of CNM7.5-0 when the content of lattice oxygen in nickel catalyst was low. However, the graphitic layers in the small, short and winding CNFs from CNM7.5-41.7 were random orientation to the CNF axis (Fig. 8b). The interlayer spacing between graphitic layers was about 0.34 nm.

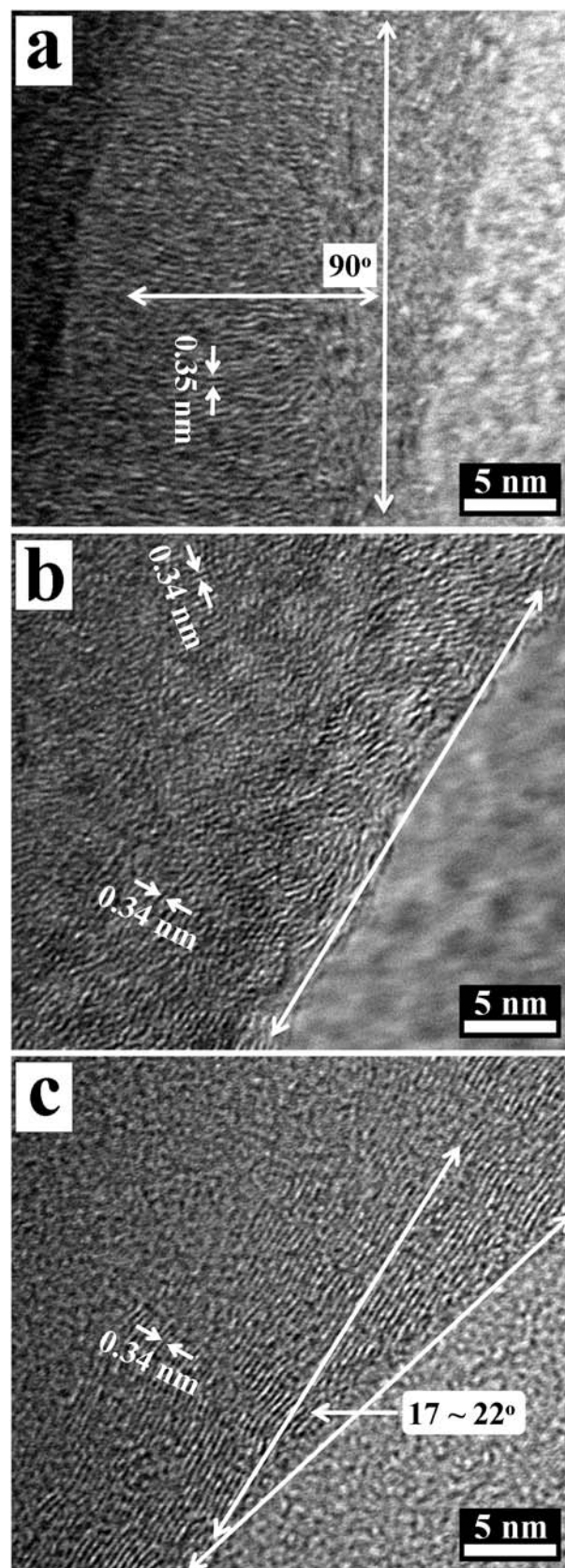


Fig. 8 HRTEM images of CNMs: (a) CNM7.5-0, (b) CNM7.5-41.7 and (c) CNM7.5-100.

Notably, the graphitic layers in the long, straight and smooth-

surface CNTs from CNM7.5-100 were oblique to the CNT axis at the angle of 17–22° (Fig. 8c). Hence, the obtained CNTs are identified as CS-CNTs, of which a large portion of exposed and reactive edges with abundant dangling bonds exist on the outer surface and in the inner channel. This makes them excellent candidates in nanoelectronics,³⁷ absorbent,³⁸ nanocomposite,³⁹ energy,⁴⁰ electrochemical biosensor,^{41,42} and catalysis.⁴³ CS-CNTs are different from herringbone CNFs,⁴⁴ since the catalyst for the growth of CNM7.5-100 (or CNM7.5-99.6) is in the molten state rather than solid state.⁴⁵ Moreover, the interlayer spacing between graphitic layers in the CS-CNTs was about 0.34 nm, consistent with the ideal graphitic interlayer spacing. Therefore, the lattice oxygen in nickel catalyst remarkably affected the morphology and microstructure of CNMs from the catalytic carbonization of PP.

3.4 Effects of lattice oxygen on the phase structure and thermal stability of CNMs

XRD, Raman and TGA measurements were employed to further study the effects of lattice oxygen content on the phase structure and thermal stability of CNMs. Fig. 9 displays the XRD patterns of both graphite (2 θ = 26.2° (002) and 42.9° (101)) and metallic Ni (2 θ = 44.5° (111), 51.9° (200) and 76.5° (220)) were observed. This indicated that NiO was reduced into metallic nickel during the growth of CNFs or CS-CNTs. The appearance of weak diffraction peaks of NiO in the CNM7.5-0 and CNM7.5-15.6 were probably due to the oxidation of nickel catalyst by air during the cooling process. Furthermore, the intensity ratio of diffraction peak of graphite (002) to that of metallic Ni (111) in CNM7.5-100, CNM7.5-99.6, CNM7.5-80.6 or CNM7.5-41.7 was obviously larger than that from CNM7.5-15.6 or CNM7.5-0. This suggested that CS-CNTs and CNFs contained less lattice distortions than PL-CFs, agreeing with the HRTEM observations (Fig. 8). Fig. S6 presents the Raman spectra of the corresponding CNMs. The peak at about 1580 cm⁻¹ (*G* band) corresponds to an *E*_{2g} mode of hexagonal graphite and is related to the vibration of sp²-bonded carbon atoms in a graphite layer, and the *D* band at about 1345 cm⁻¹ is associated with vibration of carbon atoms with dangling bonds in the plane terminations of disordered graphite or glassy carbons.^{46,47} The *I*_G/*I*_D value of CNM7.5-100 (0.58) or CNM7.5-99.6 (0.56) was obviously larger than CNM7.5-80.6 (0.53), CNM7.5-41.7 (0.52), CNM7.5-15.6 (0.49) or CNM7.5-0 (0.46). Hence, CNM7.5-100 (or CNM7.5-99.6) had relatively lower defects inside the graphite sheets than CNM7.5-80.6, CNM7.5-41.7, CNM7.5-15.6 or CNM7.5-0.

TGA was used to measure thermal stability of CNMs. Higher oxidation temperature is always associated with less defective CNMs. Fig. S7 shows the DTG curves of the CNMs under air flow at a heating rate of 10 °C/min. CNM7.5-100 or CNM7.5-99.6 showed higher maximum oxidation temperature than CNM7.5-80.6, CNM7.5-41.7, CNM7.5-15.6 or CNM7.5-0, revealing the formation of well graphitized CNMs, and/or less amorphous carbon when the content of lattice oxygen increased. The above results demonstrated that the lattice oxygen in the nickel catalyst facilitated the formation of well graphitized CNMs, and/or prevented the formation of amorphous carbon during the catalytic carbonization of PP.

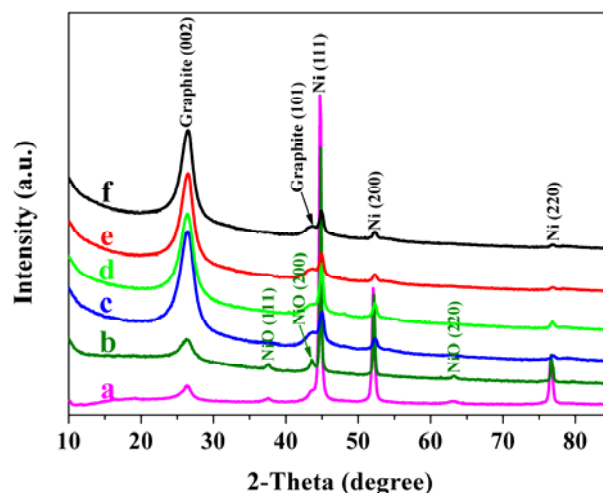


Fig. 9 XRD patterns of CNMs: (a) CNM7.5-0, (b) CNM7.5-15.6, (c) CNM7.5-41.7, (d) CNM7.5-80.6, (e) CNM7.5-99.6 and (f) CNM7.5-100.

3.5 Effects of lattice oxygen on the coalescence and reconstruction of nickel catalyst nanoparticles

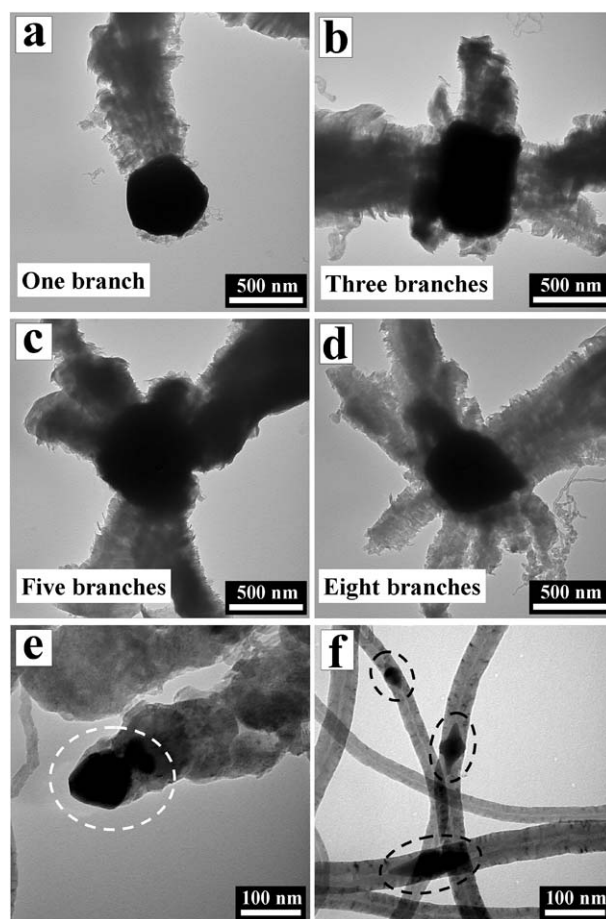


Fig. 10 TEM images of metallic nickel catalysts in PL-CFs from CNM7.5-0 (a–d), CNFs from CNM7.5-41.7 (e), and CS-CNTs from CNM7.5-100 (f).

Prior to the growth of CNMs, the catalyst nanoparticles always undergo coalescence and reconstruction, and adopt well-defined geometric shapes.⁴⁸ Correlating the content of lattice oxygen in nickel catalyst with the yield, morphology and microstructure of

CNMs is of great importance for understanding the role of lattice oxygen in the formation of CNMs. The following questions are urgent to be answered: How does the lattice oxygen influence the coalescence and reconstruction of nickel catalyst nanoparticles?

How does the lattice oxygen affect the carbonization of PP degradation products? To answer the first question, we observed the morphologies of metallic nickel catalysts in the PL-CFs, CNFs and CS-CNTs. Interestingly, the metallic nickel catalysts in the large and short PL-CFs or short, winding and rugged-surface CNFs displayed irregular polyhedral shape on the tips of PL-CFs or CNFs. However, most of the metallic nickel catalysts in the long, straight and smooth-surface CS-CNTs had rhombic shape and existed in the middle of CS-CNTs. Fig. 10 presents the TEM micrographs of the typical irregular polyhedral-shape Ni catalyst on the tip of PL-CFs from CNM7.5-0, irregular polyhedral-shape Ni catalyst on the tip of CNFs from CNM7.5-41.7 and rhombic-shape Ni catalyst in the middle of CS-CNTs from CNM7.5-100. For PL-CFs, the irregular polyhedral-shape Ni catalyst had a diameter range of 300–500 nm (Figs. 10a–10d), much larger than the mean diameter of Cat-1.0 (25.2 nm), which was obviously ascribed to the coalescence and sintering of metallic nickel nanoparticles.⁴⁹ Interestingly, a different number of branches were observed onto the coalesced nickel particles, suggesting the formation of octopus-like CFs. Similar results were observed by other researchers. Jeong and Lee⁵⁰ found that the octopus-like carbon filaments were formed on Ni particles greater than 100 nm in diameter. Comparatively, the diameter of irregular polyhedral-shape Ni catalyst in CNFs was in the range of 40–100 nm (Fig. 10e), much smaller than that in CNM7.5-0, and amorphous carbon covered some part of Ni catalysts. Strikingly, the diameter of rhombic-shape Ni catalyst in CS-CNTs was between 25 and 60 nm (Fig. 10f), lower than that in CNM-41.7, and the graphene layers near the surface of rhombic-shape Ni catalyst were parallel to the surface of rhombic-shape Ni catalyst (Fig. S8). Similar phenomena were observed by Janowska *et al.*⁵¹ They found the shape of FeN_x catalyst showed an obvious impact on the structure of carbon nanofilaments.

Consequently, the coalescence and reconstruction of nickel catalyst nanoparticles during the growth of PL-CFs, CNFs and CS-CNTs were different. Since the diameter of Cat-x (x = 1–5) was similar and the carbon sources (*i.e.*, the degradation products of PP under the catalysis of CuBr) were the same, it was speculated that the lattice oxygen promoted the reconstruction of nickel catalyst nanoparticles and prevented their coalescences into large particles during the carbonization.

3.6 Effect of lattice oxygen on the carbonization of PP degradation products

The degradation products of PP are the carbon feedstocks for the growth of PL-CFs, CNFs and CS-CNTs. In our previous reports,^{16,18,19} it was proved that a trace of halogenated compound facilitated the dehydrogenation and aromatization of PP radical fragments into a large amount of light hydrocarbons and a relative small amount of aromatics, in which propylene and toluene were the main component, respectively. Thus, to study the effect of lattice oxygen on the carbonization of PP degradation products, propylene (P), toluene (T) and their mixtures were used as carbon sources, respectively, and Cat-x

containing different content of lattice oxygen was used as carbonization catalyst in model carbonization experiment (Fig. S9). The results are shown in Fig. 11. As can be seen, no matter what kind of carbon sources was added, the carbon conversion, which was calculated by dividing the amount of carbon product after the model carbonization experiment by that of carbon element in the carbon source, increased with the increasing content of lattice oxygen. Similar phenomenon was observed by Qian *et al.*³⁰ Based on the above results, we speculated that the combination of lattice oxygen with hydrogen and carbon favored for the decomposition of light hydrocarbons and aromatics. This was why the yield of CNMs from PP/CuBr-Cat-x-y increased significantly with the increasing content of lattice oxygen (Fig. 4).

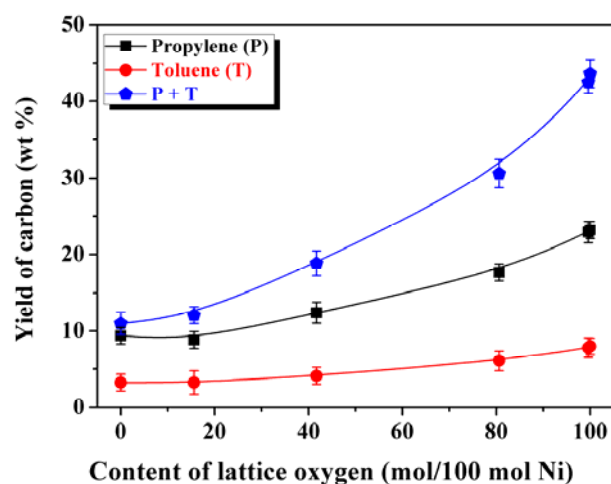


Fig. 11 Yield of carbon using different carbon source under the catalysis of Cat-x (0.10 g) with different content of lattice oxygen at 700 °C. Propylene (P) was added at 200 mL/min for 6 min, 2.5 g toluene (T) was evenly added within 6 min, or propylene was added at 100 mL/min for 6 min while 1.25 g toluene was evenly added within 6 min.

The possible mechanisms about the effect of lattice oxygen in the nickel catalyst on the catalytic carbonization of PP into CNMs including PL-CFs, CNFs and CS-CNTs are shown in Fig. 12. When the content of lattice oxygen was low, the nickel catalyst nanoparticles were coalesced into large irregular polyhedral-shape particles (step 1 in Fig. 12a), which catalyzed the degradation products of PP into graphene layers on the surface of catalyst (step 2 in Fig. 12a). As a result, PL-CFs with the graphene platelets almost perpendicularly to the fiber axis were formed (steps 3 and 4 in Fig. 12a). When the content of lattice oxygen increased, irregular polyhedral-shape nickel catalyst with smaller size than that in the PL-CFs was formed (step 1 in Fig. 12b), which was ascribed to the lattice oxygen preventing the coalescence of nickel catalyst nanoparticles. Amorphous carbon covered some part of catalyst, and the dehydrogenation and aromatization of light hydrocarbons and aromatics into graphene nanosheets only occurred on the uncovered parts of Ni catalyst from the reduction of NiO (step 2 in Fig. 12b). Finally, short, winding and rugged-surface CNFs were obtained (steps 3 and 4 in Fig. 12b). When the content of lattice oxygen further increased, the lattice oxygen promoted the reconstruction of NiO nanoparticles into rhombic-shape NiO catalyst with much smaller size compared to that in the CNFs (step 1 in Fig. 12c), which catalyzed light hydrocarbons and aromatics into graphene

nanosheets on the middle surface of reshaped Ni catalyst from the reduction of NiO (step 2 in Fig. 12c). These graphene nanosheets were parallel to the surface of the rhombic-shape Ni catalyst (Fig. S8) and assembled to gradually construct the CS-CNT structure.

This was the reason why the graphene layers in the CS-CNTs were oblique to the CS-CNTs axis at the angle of 17–22° (Fig. 8). Finally, CS-CNTs grew up from the two ends of rhombic-shape Ni catalyst until the reaction was over (steps 3 and 4 in Fig. 12c).

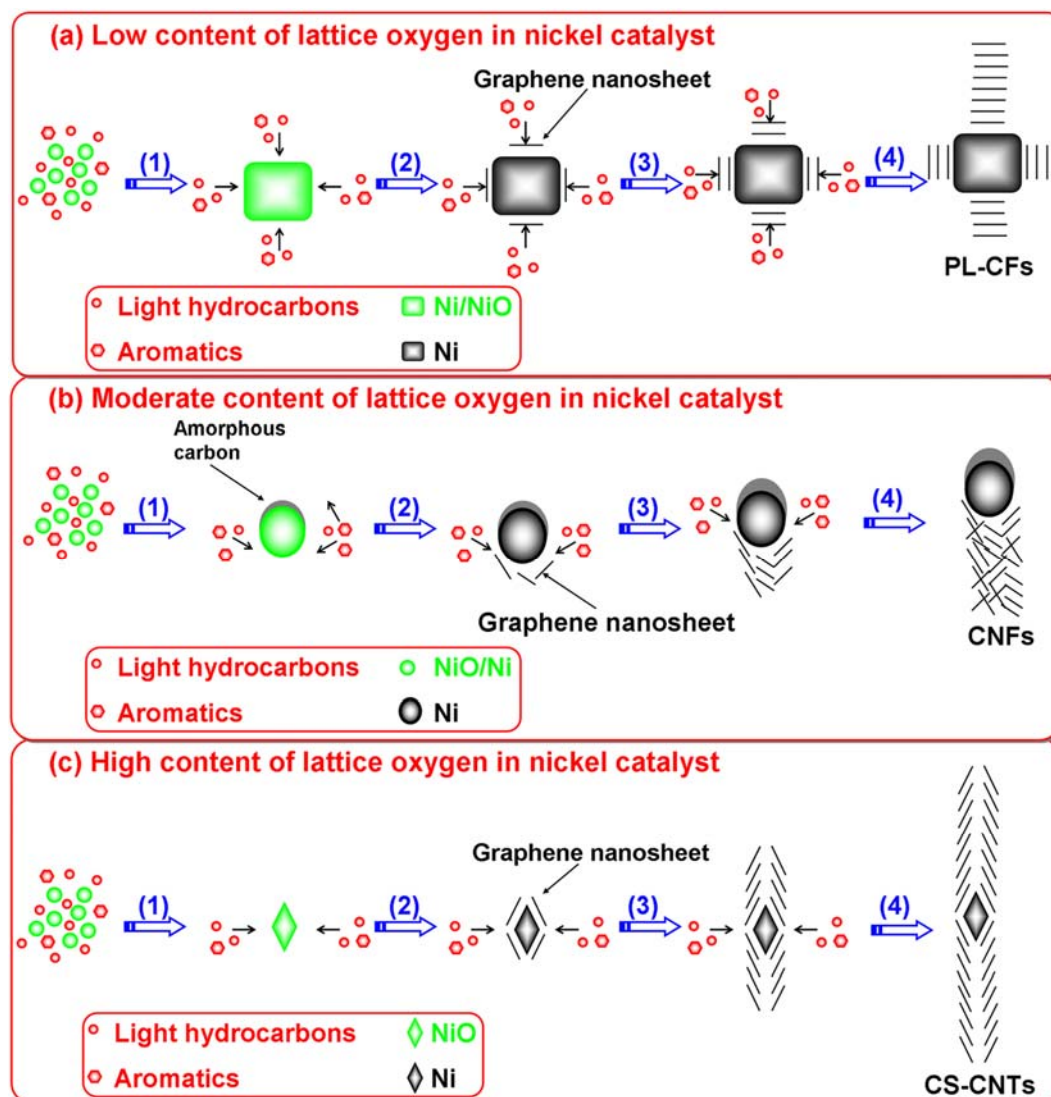


Fig. 12 Possible mechanisms about the effect of lattice oxygen in the nickel catalyst on the catalytic carbonization of PP into CNMs including PL-CFs (a), CNFs (b) and CS-CNTs (c).

4. Conclusions

Uniform nickel catalyst with different content of lattice oxygen but similar diameter was prepared by controlling the molar ratio of $\text{Ni}(\text{NO}_3)_2$ to citric acid using sol-gel combustion synthesis method. The combined CuBr/nickel catalysts showed a synergetic effect on the carbonization of PP into carbon nanomaterials including platelet-like carbon fibers, carbon nanofibers and cup-stacked carbon nanotubes at 700 °C. The yield of carbon nanomaterials increased dramatically with the increasing content of lattice oxygen. Large and short platelet-like carbon fibers were obtained when the content of lattice oxygen was low (e.g., 15.6 mol/100 mol Ni). When the content of lattice oxygen increased (e.g., 80.6 mol/100 mol Ni), small, winding and

short carbon nanofibers were produced. However, when the content of lattice oxygen further increased (e.g., 99.6 mol/100 mol Ni), long and straight cup-stacked carbon nanotubes were formed. In addition, it was demonstrated that the lattice oxygen not only promoted the reconstruction of nickel nanoparticles into rhombic shape and prevented their coalescences into large particles, but also facilitated the carbonization of polypropylene degradation products. We hope this work will provide more insights into the carbonization mechanism of polyolefin and contribute to the preparation of valuable carbon nanomaterials with diverse morphologies.

Acknowledgements

We would like to thank the reviewers for kind and important

suggestions. This work was supported by the National Natural Science Foundation of China (51373171, 21204079, 51233005 and 21374114) and Polish Foundation (No. 2011/03/D/ST5/06119).

5 Notes and references

^a State Key Laboratory of Polymer Physics and Chemistry, Changchun Institute of Applied Chemistry, Chinese Academy of Sciences, Changchun 130022, China. Fax: +86 (0) 431 85262827; Tel: +86 (0) 431 85262004; E-mail: ttang@ciac.ac.cn; xchen@ciac.ac.cn

^b University of Chinese Academy of Sciences, Beijing 100049, China

^c Institute of Chemical and Environment Engineering, West Pomeranian University of Technology, Szczecinul. Pulaskiego 10, 70-322 Szczecin, Poland

† Electronic Supplementary Information (ESI) available: FE-SEM

images of nickel catalysts, the diameter distributions of nickel catalysts, TGA and DTG curves of nickel catalysts, the length distributions of CNMs, the diameter distributions of CNMs, Raman spectra of CNMs, DTG curves of CNMs, HRTEM image of rhombic-shape Ni catalyst, and schematic diagram of the model carbonization experiment. See DOI: 10.1039/b000000x/

References

- 1 C. W. Zhuo and Y. A. Levendis, *J. Appl. Polym. Sci.*, 2014, **131**, 39931–39944.
- 2 R. Soheilian, A. Davies, S. T. Anaraki, C. W. Zhuo and Y. A. Levendis, *Energ. Fuel.*, 2013, **27**, 4859–4868.
- 3 P. T. Williams and E. Slaney, *Resour. Conserv. Recycl.*, 2007, **51**, 754–769.
- 4 C. F. Wu and P. T. Williams, *Appl. Catal. B: Environ.*, 2009, **90**, 147–156.
- 5 D. P. Serrano, J. Aguado and J. M. Escola, *ACS Catal.*, 2012, **2**, 1924–1941.
- 6 C. F. Wu, Z. C. Wang, L. Z. Wang, P. T. Williams and J. Huang, *RSC Adv.*, 2012, **2**, 4045–4047.
- 7 C. F. Wu, M. A. Nahil, N. Miskolczi, J. Huang and P. T. Williams, *Environ. Sci. Technol.*, 2014, **48**, 819–826.
- 8 J. C. Acomb, C. F. Wu and P. T. Williams, *Appl. Catal. B: Environ.*, 2014, **147**, 571–584.
- 9 C. W. Zhuo, B. Hall, H. Richter and Y. Levendis, *Carbon*, 2010, **48**, 4024–4034.
- 10 C. W. Zhuo, J. O. Alves, J. A. S. Tenorio and Y. A. Levendis, *Ind. Eng. Chem. Res.*, 2012, **51**, 2922–2930.
- 11 C. W. Zhuo, X. Wang, W. Nowak and Y. A. Levendis, *Appl. Surf. Sci.*, 2014, **313**, 227–236.
- 12 V. G. Pol and M. M. Thackeray, *Energy Environ. Sci.*, 2011, **4**, 1904–1912.
- 13 T. Tang, X. C. Chen, X. Y. Meng, H. Chen and Y. P. Ding, *Angew. Chem. Int. Ed.*, 2005, **44**, 1517–1520.
- 14 Z. W. Jiang, R. J. Song, W. G. Bi, J. Lu and T. Tang, *Carbon*, 2007, **45**, 449–458.
- 15 R. J. Song, Z. W. Jiang, W. G. Bi, W. X. Cheng, J. Lu, B. T. Huang and T. Tang, *Chem. Eur. J.*, 2007, **13**, 3234–3240.
- 16 J. Gong, J. Liu, Z. W. Jiang, X. Wen, X. C. Chen, E. Mijowska, Y. H. Wang and T. Tang, *Chem. Eng. J.*, 2013, **225**, 798–808.
- 17 J. Gong, J. Liu, L. Ma, X. Wen, X. C. Chen, D. Wan, H. O. Yu, Z. W. Jiang, E. Borowiak-Palen and T. Tang, *Appl. Catal. B: Environ.*, 2012, **117–118**, 185–193.
- 18 J. Gong, J. Liu, Z. W. Jiang, J. D. Feng, X. C. Chen, L. Wang, E. Mijowska, X. Wen and T. Tang, *Appl. Catal. B: Environ.*, 2014, **147**, 592–601.
- 19 J. Gong, J. D. Feng, J. Liu, Z. W. Jiang, X. C. Chen, E. Mijowska, X. Wen and T. Tang, *Chem. Eng. J.*, 2014, **48**, 27–40.
- 20 J. Gong, J. Liu, D. Wan, X. C. Chen, X. Wen, E. Mijowska, Z. W. Jiang, Y. H. Wang and T. Tang, *Appl. Catal. A: Gen.*, 2012, **449**, 112–120.
- 21 J. Gong, J. Liu, Z. W. Jiang, X. C. Chen, X. Wen, E. Mijowska and T. Tang, *Appl. Catal. B: Environ.*, 2014, **152–153**, 289–299.
- 22 Z. H. Guan, S. M. Lu, Z. J. Chen and C. Li, *J. Catal.*, 2013, **305**, 19–26.
- 23 D. N. Futaba, J. Goto, S. Yasuda, T. Yamada, M. Yumura and K. Hata, *J. Am. Chem. Soc.*, 2009, **131**, 15992–15993.
- 24 D. N. Futaba, J. Goto, S. Yasuda, T. Yamada, M. Yumura and K. Hata, *Adv. Mater.*, 2009, **21**, 4811–4815.
- 25 O. Guellati, I. Janowska, D. Bégin, M. Guerioune, Z. Mekhalif, J. Delhalle, S. Moldovan, O. Ersen and C. Pham-Huu, *Appl. Catal. A: Gen.*, 2012, **423–424**, 7–14.
- 26 F. Ren, S. A. Kanaan, M. M. Majewska, G. D. Keskar, S. Azoz, H. Wang, X. M. Wang, G. L. Haller, Y. Chen and L. D. Pfefferle, *J. Catal.*, 2014, **309**, 419–427.
- 27 C. Z. Loebick, R. Podila, J. Reppert, J. Chudow, F. Ren, G. L. Haller, A. M. Rao and L. D. Pfefferle, *J. Am. Chem. Soc.*, 2010, **132**, 11125–11131.
- 28 C. Z. Loebick, S. Derrouiche, F. Fang, N. Li, G. L. Haller and L. D. Pfefferle, *Appl. Catal. A: Gen.*, 2009, **368**, 40–49.
- 29 B. L. Liu, D. M. Tang, C. H. Sun, C. Liu, W. C. Ren, F. Li, W. J. Yu, L. C. Yin, L. L. Zhang, C. B. Jiang and H. M. Cheng, *J. Am. Chem. Soc.*, 2011, **133**, 197–199.
- 30 W. Z. Qian, T. Liu, F. Wei, Z. W. Wang and Y. D. Li, *Appl. Catal. A: Gen.*, 2004, **258**, 121–124.
- 31 Z. J. Fan, J. Yan, T. Wei, G. Q. Ning, L. J. Zhi, J. C. Liu, D. X. Cao, G. L. Wang and F. Wei, *ACS Nano*, 2011, **5(4)**, 2787–2794.
- 32 M. Tsuji, M. Kubokawa, R. Yano, N. Miyamae, T. Tsuji, M. S. Jun, S. Hong, S. Lim, S. H. Yoon and I. Mochida, *Langmuir*, 2007, **23**, 387–390.
- 33 C. A. Bessel, K. Laubernds, N. M. Rodriguez and R. T. K. Baker, *J. Phys. Chem. B*, 2001, **105**, 1115–1118.
- 34 M. Takasaki, Y. Motoyama, K. Higashi, S. H. Yoon, I. Mochida and H. Nagashima, *Org. Lett.*, 2008, **10(8)**, 1601–1604.
- 35 J. S. Zheng, X. S. Zhang, P. Li, X. G. Zhou and W. K. Yuan, *Catal. Today*, 2008, **131**, 270–277.
- 36 Y. W. Jiang, S. G. Yang, Z. H. Hua and H. B. Huang, *Angew. Chem. Int. Ed.*, 2009, **121**, 8681–8683.
- 37 Q. F. Liu, W. C. Ren, Z. G. Chen, L. C. Yin, F. Li, H. T. Cong and H. M. Cheng, *Carbon*, 2009, **47**, 731–736.
- 38 J. Gong, J. Liu, X. C. Chen, Z. W. Jiang, X. Wen, E. Mijowska and T. Tang, *RSC Adv.*, 2014, **4**, 33806–33814.
- 39 T. Yokozeki, Y. Iwahori, S. Ishiwata and K. Enomoto, *Compos. Sci. Technol.*, 2009, **69**, 2268–2273.
- 40 I. Y. Jang, H. Ogata, K. C. Park, S. H. Lee, J. S. Park, Y. C. Jung, Y. J. Kim, Y. A. Kim and M. Endo, *J. Phys. Chem. Lett.*, 2010, **1**, 2099–2103.
- 41 S. Ko, Y. Takahashi, H. Fujita, T. Tatsuma, A. Sakoda and K. Komori, *RSC Adv.*, 2012, **2**, 1444–1449.
- 42 S. Ko, T. Tatsuma, A. Sakoda, Y. Sakai and K. Komori, *Phys. Chem. Chem. Phys.*, 2014, **16**, 12209–2213.
- 43 K. Saito, M. Ohtani and S. Fukuzumi, *J. Am. Chem. Soc.*, 2006, **128**, 14216–14217.
- 44 G. B. Zheng, K. Kouda, H. Sano, Y. Uchiyama, Y. F. Shi and H. J. Quan, *Carbon*, 2004, **42**, 635–640.
- 45 Y. A. Kim, T. Hayashi, S. Naokawa, T. Yanagisawa and M. Endo, *Carbon*, 2005, **43**, 3002–3039.
- 46 C. F. Wu, J. Huang and P. T. Williams, *RSC Adv.*, 2013, **3**, 19239–19242.
- 47 P. Roy, A. P. Periasamy, C. Chuang, Y. R. Liou, Y. F. Chen, J. Joly, C. T. Liang and H. T. Chang, *New J. Chem.*, 2014, **38**, 4946–4951.
- 48 N. M. Rodriguez, A. Chambers and R. T. K. Baker, *Langmuir*, 1995, **11**, 3862–3866.
- 49 A. T. DeLaRiva, T. W. Hansen, S. R. Challa and A. K. Datye, *J. Catal.*, 2013, **308**, 291–305.
- 50 N. Jeong and J. Lee, *J. Catal.*, 2008, **260**, 217–226.
- 51 W. Baaziz, G. Melinte, O. Ersen, C. Pham-Huu and I. Janowska, *Phys. Chem. Chem. Phys.*, 2014, **16**, 15988–15993.